Solid State Communications 289 (2019) 61–66

Contents lists available at ScienceDirect

Solid State Communications

journal homepage: www.elsevier.com/locate/ssc

Communication

Edge modification induced giant rectification effect in armchair C_2N-*h*2D nanoribbons

Jing-Jing He[a,b], Yan-Dong Guo[a,b,*], Xiao-Hong Yan[a,b,c,d,**], Hong-Li Zeng[b,e], Yang Ni[a,b]

[a] College of Electronic and Optical Engineering, Nanjing University of Posts and Telecommunications, Nanjing 210046, China
[b] Key Laboratory of Radio Frequency and Micro-Nano Electronics of Jiangsu Province, Nanjing, 210023, Jiangsu, China
[c] College of Science, Nanjing University of Aeronautics and Astronautics, Nanjing 210016, China
[d] School of Material Science and Engineering, Jiangsu University, Zhenjiang 212013 China
[e] College of Natural Science, Nanjing University of Posts and Telecommunications, Nanjing 210023, China

ARTICLE INFO

Communicated by L. Brey

Keywords:
Electronic transport
Rectification effect
Density-functional theory
Nonequilibrium Green's function

ABSTRACT

The recently synthesized two-dimensional C_2N-*h*2D material has received extensive attention due to its similar honeycomb structure with graphene as well as uniform distribution of nitrogen atoms and holes. We perform first-principles calculations and find that armchair C_2N-*h*2D nanoribbon (AC_2NNR) is quite sensitive to edge modification. Edge unmodified and H-modified AC_2NNRs are direct band gap semiconductors, while O-modified becomes an indirect band gap semiconductors. Interestingly, when both edge and sub-edge are modified with H or O atoms, it turns into a metal. Metal-semiconductor heterojunctions constructed from property-distinctive AC_2NNRs all exhibit forward-blocking and reverse-conducting rectifying diode behaviors, and the maximum rectification ratio reaches an incredible value of 10^{10}, showing good application prospects.

1. Introduction

Among the methods for regulating the electronic properties of nanoribbons such as doping, adsorption, and reconstruction, edge modification has been a hot topic for many research groups [1–9]. Bare zigzag graphene nanoribbons (ZGNRs) is metallic with two degenerate bands crossing the Fermi level which are more than half filled based on LDA method [10]. For monohydrogenated graphene nanoribbon (sp^2 σ-bonded edge C), early tight-binding studies have shown that the ideal ZGNR is metallic and independent of the ribbon width, while the ideal armchair graphene nanoribbon (AGNR) has width-relevant band gap [11]. If terminated by two H atoms, ZGNR becomes more stable, and bandgap opening and magnetism disruption can be observed [12]. Lee et al. [10] find that the oxidation of the OH group produces almost the same band structure as the monohydrogenation (sp^2 hybridization) does, and that the ketone CO and ether C2O groups are similar to the dihydrogenation (sp^3 hybridization), always making edge-modified ZGNR metallic due to the difference in electronegativity of the edge C and O atoms. The edge functionalizations of NH_2, OH, COOH, and S-NO_2 result in spin-selective semiconductivity, but O and MS-NO_2 form a semiconductor-to-metal transition [13]. Graphene-based nanoribbon heterostructures have attracted considerable attention because they can integrate a variety of useful effects such as rectification, giant magnetoresistance, spin filters and spin caloritronics [14–19]. Cao et al. [20] report that bare-monohydrogenated ZGNR heterojunction has better conductivity, while both bare-dihydrogenated and monohydrogenated-dihydrogenated ZGNR heterojunctions exhibit rectification characteristics caused by the different mirror operation symmetry of the bands near the Fermi level. Similar heterojunctions have also been found to exhibit rectifying properties in nanoribbons of other graphene-like two-dimensional materials. For example, partially edge-hydrogenated MoS_2 nanoribbon heterostructure [14] and bare-monohydrogenated phosphorene heterojunction [21]. In the previous work, most efforts are devoted to the edge modification to regulate the properties of the zigzag nanoribbons due to the lack of edge state near Fermi level in the armchair nanoribbons [13]. However, in this paper, we focus on the armchair nanoribbon of the new two-dimensional C_2N-*h*2D material [22–27]. The results show that the edge modification can effectively regulate its electronic property, and realize semiconductor-to-metal transition. A rectification ratio up to 10^{10} is achieved in designed metal-semiconductor contact heterojunction, showing great potential for application in future nanodevices.

* Corresponding author. No. 9 Wenyuan Road, Qixia District, Nanjing 210046, China.
** Corresponding author. No. 9 Wenyuan Road, Qixia District, Nanjing 210046, Chinaa.
E-mail addresses: yandongguo@njupt.edu.cn (Y.-D. Guo), yanxh@njupt.edu.cn (X.-H. Yan).

https://doi.org/10.1016/j.ssc.2018.12.012
Received 27 July 2018; Received in revised form 30 October 2018; Accepted 14 December 2018
Available online 17 December 2018

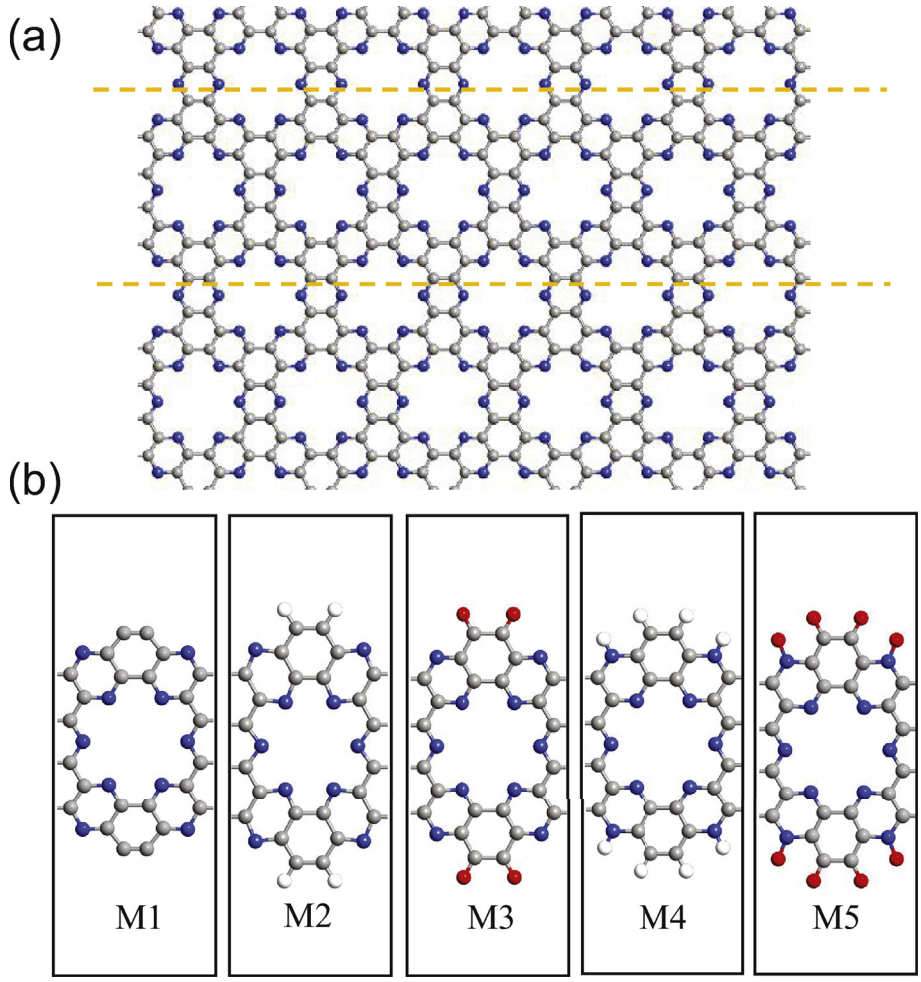

Fig. 1. Schematic illustrations of (a) monolayer C_2N-*h*2D material; (b) AC_2NNRs with different edge modifications after optimization, M1 to M3 models are successively edge non-passivated, H-passivated, and O-passivated, while M4 or M5 models are respectively edge and sub-edge H-passivated or O-passivated. Nitrogen, carbon, hydrogen, and oxygen atoms are represented by blue, gray, white, and red balls, separately. (For interpretation of the references to colour in this figure legend, the reader is referred to the Web version of this article.)

2. Computational method

The calculations are performed by the atomistix Toolkit (ATK) package, which is based on the combination of density functional theory (DFT) and non-equilibrium Green's function (NEGF) technique [28]. The Perdew-Burke-Eenzerhof formulation of the generalized gradient approximation (GGA) is used as the exchange-correlation function, and the double-zeta polarized basis set is employed in the calculations. The mesh cutoff energy is set to be 150 Ry, and a Monkhorst-Pack *k*-point mesh of $1 \times 1 \times 13$ is used for the one-dimensional Brillouin zone of AC_2NNR nanoribbon, and $1 \times 1 \times 100$ for AC_2NNR two-probe nanodevice [29]. The vacuum spaces of supercell are set to be more than 15 Å to eliminate the interactions between periodic adjacent images. All the atomic positions of the structure have been optimized until all the forces are less than 0.01 eV/Å.

3. Results and discussions

Due to the heterogeneity of C and N elements and the presence of holes in monolayer C_2N-*h*2D material [22,23], there are various ways to be cut into nanoribbons. Cutting along the dashed lines as shown in Fig. 1(a), an armchair nanoribbon named M1 is obtained in Fig. 1(b). M1 model is edge non-passivated, to study the effect of diverse edge modification on its electronic structure, more models have been designed, such as edge H/O-passivated M2/M3, as well as edge and sub-edge H/O-passivated M4/M5 model.

In Fig. 2(a), the band structures of M1 to M5 models are calculated. Obviously, diverse edge modification results in a significant change in the electronic property of AC_2NNR. The edge non-passivated M1 structure is a direct bandgap semiconductor with a bandgap of 1.54 eV, which is slightly smaller than the 1.56 eV calculated by Wang et al. based on VASP [30]. After passivated by H atoms (M2), it is still a direct bandgap semiconductor, but the bandgap is reduced to 1.20 eV. However, if edge is passivated by O atoms (M3), it turns into an indirect bandgap semiconductor, with a conduction band minimum (CBM) located at Γ-point and a valence band maximum (VBM) moving to Z point, resulting a reduce in bandgap to 0.81 eV, which is different from the metallicity of O-terminated ZGNR [10]. Interestingly, when both edge and sub-edge are H-passivated (M4) or O-passivated (M5), a semiconductor-to-metal transition occurs. M4 is due to the falling of CBM to contact with the Fermi level, while M5 is due to the occurrence of a band crossing the Fermi level. Recently, Fan et al. [10] reported that for zigzag phosphene nanoribbon, the edge non-passivated structure exhibits metallicity, and the edge H-passivated is a semiconductor with a direct band gap of 1.44 eV, which is opposite to the edge modification effect of AC_2NNR we studied.

To clarify the change in the band structure, the distribution of the real-space wave functions of several energy bands near the Fermi level is calculated in Fig. 2(b). First looking at the $n = 1$ band, its wave function in all models has a similar distribution, mainly from the π

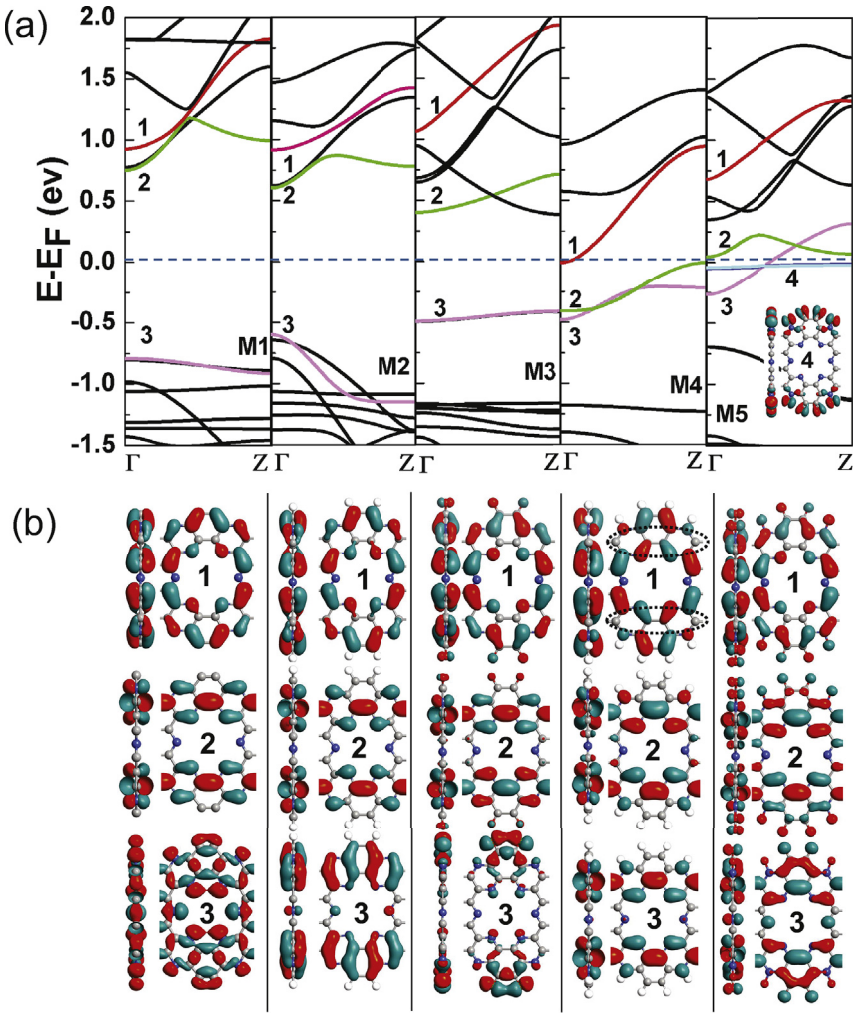

Fig. 2. (a) Band structures of M1 to M5 AC_2NNRs around the Fermi level. The dashed line is the Fermi level, and the energy bands near the Fermi level are numbered from top to bottom. (b) Side and front views of isosurface plots of the Γ-point wave functions of labeled subbands.

bonds formed by the P_z orbitals of C and N atoms, however due to the passivation effect, its energy decreases as shown in Fig. 2(a), especially in the M4 model, it drops to contact with the Fermi level to make M4 a metal, which may derive from the contributions of the central C atoms instead of the side C atoms in the third row as marked by a circle. For the n = 2 band, the state appears to be along the ribbon direction, unlike n = 1 band whose state is more oriented across the ribbon. In the M1 model, its wave function comes from the contributions of the P_z orbitals of C and N atoms, excluding the edge and central atoms. After the H-modification, the contributions of the C atoms in the center of the sub-edge are weakened, and after the O-modification, the P_z orbital of O atom also participates in the contribution, which may result in the energy reduction of n = 2 band in Fig. 2(a).

Observing the n = 3 band, its wave functions distributes differently in these five models. In M1 model, its state is delocalized, which comes from the σ bonds formed by s orbitals of all atoms [22]. However, in other models, the contributions of the central C atoms are suppressed. For example, in M2 model its state derives from the P_z orbitals of other atoms, and in M3 model, it is obviously localized at the edge C and O atoms indicating an edge state, and it is precisely because the VBM of this edge state is at the Z point that the M3 model becomes an indirect bandgap semiconductor. In M4 model, it behaves like n = 2 band except the central C atoms. In M5 model, the P_z orbitals of all atoms excluding the central C atom are involved in the hybridization, especially the edge O atoms, finally the n = 3 band passes through the Fermi level, making the M5 structure a metal. In addition, there are two degenerate bands near the Fermi level, as can be seen from the inset of Fig. 2(a) (the other band has similar wave function, for clarity, not shown here), their wave functions are localized at the edge and sub-edge O atoms belonging to edge states.

Metallic M4, M5 and semiconductor M1-M3 are respectively selected to construct metal-semiconductor contact nanodevices, i.e., M4-M1, M5-M1 and M4-M2 heterostructures as presented in Fig. 3(a) and the insets of Fig. 3(b). Their current-voltage characteristics (*I-V*) are calculated in Fig. 3(b). Obviously, their *I-V* curves all show forward-blocking and reverse-conducting rectifier diode characteristics (the M4-M2 device is difficult to converge at the bias of −0.6 V, so its current value at −0.6 V is not shown). In the bias range of −0.7 V to −1.0 V, these three devices conduct and their currents increase as the bias increases. Among them, under the same conducting reverse bias, the current value of M4-M2 device is greater than that of M4-M1 and M5-M1, and reaches the maximum of 3.5 μA at 1.0 V.

Table 1 represents the specific rectification ratio of these three devices in the bias range from 0 to 1.0 V (the rectification ratio of a certain bias here is defined as the absolute value of the ratio of the current at reverse bias to that at forward bias). As can be seen, in the conduction bias range of 0.7–1.0 V, the M4-M1 device has a high rectification ratio of 4.66×10^6 at 0.8 V, while that of M5-M1 is higher achieving 2.69×10^{10} at 0.9 V, which is much higher than those reported by other research teams, exhibiting outstanding rectification performance [31–35].

In NEGF theory, the current of the two-probe system is calculated

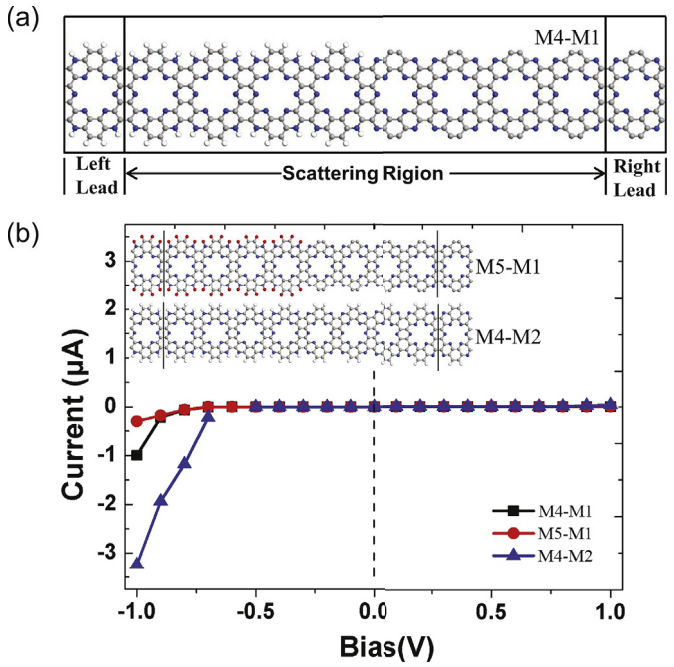

Fig. 3. (a) Schematic illustration of M4-M1 two-probe nanodevice constructed of M4 and M1 structures. Two-probe device is divided into three parts: semi-infinite left electrode, central scattering region and semi-infinite right electrode. Vacuum layer is not shown for clarity. (b) The current-voltage curves of M4-M1, M5-M1 and M4-M2 devices in the bias range from −1.0–1.0 V. The inset above is a schematic of the M5-M1 two-probe nanodevice constructed of M5 and M1 structures; the inset below is a schematic of the M4-M2 two-probe nanodevice constructed of M4 and M2 structures.

Table 1
Rectification ratios of M4-M1, M5-M1, and M4-M2 devices in the bias range from 0 to 1.0 V.

Bias	M4-M1	M5-M1	M4-M2
0.1	6.08×10^1	1.13×10^2	5.46×10^1
0.2	1.35×10^3	3.21×10^3	8.27×10^2
0.3	1.22×10^5	2.76×10^5	8.71×10^2
0.4	2.25×10^6	9.63×10^4	7.80×10^2
0.5	1.79×10^8	6.85×10^6	6.70×10^3
0.6	2.61×10^9	2.33×10^9	–
0.7	2.25×10^7	1.76×10^{11}	2.51×10^3
0.8	4.66×10^6	6.77×10^8	1.96×10^2
0.9	3.83×10^5	2.69×10^{10}	1.04×10^2
1.0	6.88×10^4	3.04×10^8	8.63×10^1

based on the Landauer-Büttiker formula

$$I(V) = \frac{2e}{h} \int T(E, V)[f(E - \mu_L) - f(E - \mu_R)]dE, \quad (1)$$

where $\mu_{L(R)}$ is the chemical potential of the left (right) electrode, $f(E - \mu_{L(R)})$ is the Fermi distribution of the left (right) electrode, and $V = (\mu_L - \mu_R)/e$ represents the bias window. $T(E, V)$ is the transmission coefficient obtained by using Green's function. Clearly, the current is determined by the area of the integral region in the bias window.

In order to explore the rectification mechanism, the transmission spectra under different bias voltages represented by the M5-M1 device are shown in Fig. 4. Apparently, at 0 V, the transmission coefficient at the Fermi level is zero, showing semiconducting property, and some broad transmission peaks appear near 1.0 eV and −1.5 eV. When a forward bias is applied, as the bias increases, the transmission peaks near these two energies become narrower and farther away from the Fermi level, making the energy range with zero transmission coefficient near the Fermi level wider and wider, so the M5-M1 device is cut off.

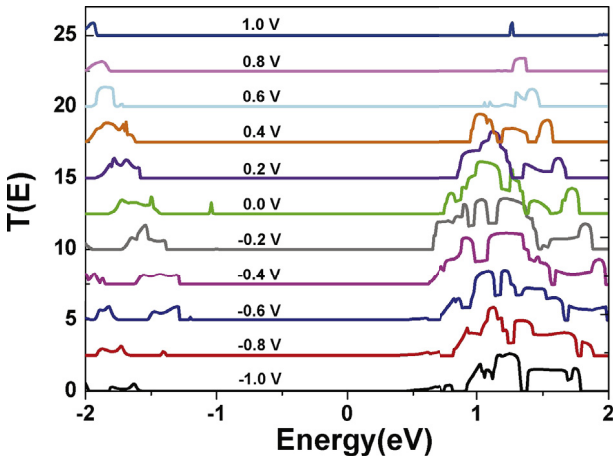

Fig. 4. The transmission spectra of M5-M1 device at different bias. Zero energy is the Fermi level.

When a reverse bias is applied, as the bias increases, the transmission peak near −1.5 eV first approaches the Fermi level and then moves away, but always fails to enter the bias window (the bias window is defined as the range from -V/2 to V/2, V is the absolute value of the bias), so does not facilitate the device conduction. In contrast, the transmission peak near 1.0 eV broadens as the reverse bias increases. After a bias higher than −0.6 V, this transmission peak enters the bias window so that electrons can be transmitted and the M5-M1 device is turned on. On the whole, from 1.0 to −1.0 V, the transmission peak near 1.0 eV gradually widens, and then enters the bias window at high reverse bias inducing a forward-blocking and reverse-conducting rectification effect.

In order to further elucidate the physical mechanism behind the transmission spectrum, the projected density of states (PDOS) plots of M5-M1 device at 0 V, 1.0 V, and −1.0 V are presented in Fig. 5. First observing the case of 0 V as shown in Fig. 5(a), the left electrode (L) has a PDOS peak at the Fermi level, corresponding to the metallicity of M5, while the PDOS of the right electrode (R) is zero within a wide energy range near the Fermi level, corresponding to the semi-conductivity of M1 with a band gap of 1.54 eV displayed in Fig. 2. After the combination of M5 and M1 AC_2NNRs, the PDOS of the central scattering region (C) also has a peak at the Fermi level, however due to the zero state density of the right electrode near the Fermi level, electrons cannot be transmitted in this device resulting in zero transmission coefficient as discussed in Fig. 4.

After applying a bias of 1.0 V, as shown in Fig. 5(b), the PDOS plots of L and C shift toward the negative energy direction compared to that at 0 V with little change in the overall shapes of the curve, however, the PDOS plot of R shifts toward the positive energy direction and changes greatly, especially the PDOS peak near −0.4 eV becomes very small in contrast to that near −0.9 eV at 0 V. In the bias window, the PDOS values of the three parts L, C, and R are all non-zero at the −0.4 eV, but since these values are so small, the probability that electrons are transmitted is quite low.

After applying a bias of −1.0 V, as shown in Fig. 5(c), compared to 0 V, the PDOS plots of L and C move toward positive energy direction, and the PDOS plot of R moves toward negative energy direction. Focusing on PDOS near 0.5 eV, both L and C have a large PDOS peak, which originates from the PDOS peak of the Fermi level at 0 V bias, noticeably, the right electrode R also has a PDOS peak due to the widening and heightening of the PDOS peak near 0.7 eV at 0 V bias. Finally electrons can be transmitted from the left electrode to the right electrode, so the transmission coefficient at −1.0 V in the bias window is not zero shown in Fig. 4, and the M5-M1 device conducts.

As for the zigzag C_2N-*h*2D nanoribbons (ZC_2NNRs), we also check the effect of the same edge modifications on their electronic structures

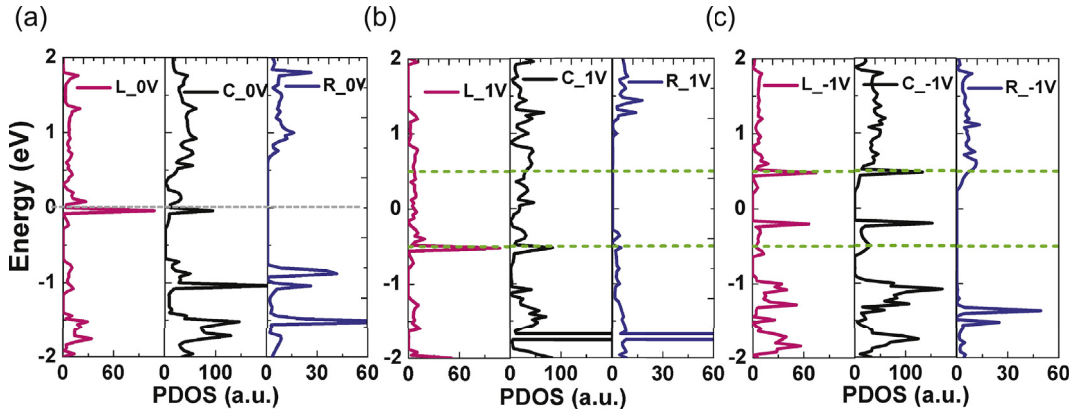

Fig. 5. Projected density of states (PDOS) plots of M5-M1 device projected on the left electrode (L), the central scattering region (C) and the right electrode (R) at (a) 0 V; (b) 1.0 V; (C) −1.0 V. The area between the green dotted lines is the bias window, and the gray dashed line is the Fermi level. (For interpretation of the references to colour in this figure legend, the reader is referred to the Web version of this article.)

and transport properties. Different from AC_2NNRs, all edge-modified ZC_2NNRs are metals, indicating that this modification method cannot effectively modulate the electronic properties of the ZC_2NNRs.

In addition, we further compare the electronic and transport properties of monohydrogenated and dihydrogenated AC_2NNRs at the same edge site, i.e., M2 and M2-2h models, as well as M4 and M4-2h models (not shown here). We find that like M2 model, M2-2h is a direct bandgap semiconductor too, but its bandgap increases to 1.68 eV compared to 1.20 eV of M2. However, M4-2h model is different from M4 model and is no longer a metal, but a semiconductor with a direct bandgap of 0.48 eV. Due to the larger band gap, M2-2h model is chosen to form M4-M2-2h device with the metallic M4 model. As a result, like M4-M2 and other devices, M4-M2-2h device also exhibits forward-blocking and reverse-conducting rectifier diode behavior, which is in line with our analysis above.

4. Conclusion

In summary, using first-principles calculations, we have studied the effects of edge modifications on the electronic structures and transport properties of the armchair C_2N-*h*2D nanoribbons (AC_2NNRs). The unmodified AC_2NNR is a semiconductor with a direct bandgap of 1.54 eV. After edge modification of H or O atoms, it remains semiconducting but its bandgap becomes a direct bandgap of 1.20 eV or an indirect bandgap of 0.81 eV. Interestingly, when both the edge and sub-edge are passivated with H atoms (M4) or O atoms (M5), AC_2NNR becomes a metal. Selecting metallic and semiconducting AC_2NNRs to construct heterojunction devices, a forward-blocking and reverse-conducting rectifier diode behavior occurs with a rectification ratio as high as 10^{10}. The transmission spectra in the range from 1.0 to −1.0 V show that the transmission peak at positive energy gradually widens, and after −0.6 V, part of the transmission peak enters the bias window, causing the device to conduct. After further analysis of PDOS, we find that the forward-blocking and reverse-conducting rectifier diode phenomenon stems from the wide bandgap of the semiconducting AC_2NNR and the opposite trend of PDOS peak in the bias window under the forward and reverse bias. Our work provides a basic theoretical guidance for the design and application of the new two-dimensional C_2N-*h*2D material in future nanoelectronic devices, especially the rectifying devices.

Acknowledgement

This work is supported by the National Natural Science Foundation of China (NSFC11504178, NSFC11374162, NSFC11247033 and NSFC51651202), the Natural Science Foundation of Jiangsu Province (BK20150825 and TJ215009), the Scientific Research Foundation of Nanjing University of Posts and Telecommunications (NY214010 and NY217013), and the Fundamental Research Funds for the Central Universities (NS2014073.

References

[1] E.-j. Kan, Z. Li, J. Yang, J. Hou, Half-metallicity in edge-modified zigzag graphene nanoribbons, J. Am. Chem. Soc. 130 (13) (2008) 4224–4225.
[2] Z. Wang, Q. Li, H. Zheng, H. Ren, H. Su, Q. Shi, J. Chen, Tuning the electronic structure of graphene nanoribbons through chemical edge modification: a theoretical study, Phys. Rev. B 75 (11) (2007) 113406.
[3] S. Dutta, A.K. Manna, S.K. Pati, Intrinsic half-metallicity in modified graphene nanoribbons, Phys. Rev. Lett. 102 (9) (2009) 096601.
[4] B. Xu, J. Yin, Y. Xia, X. Wan, K. Jiang, Z. Liu, Electronic and magnetic properties of zigzag graphene nanoribbon with one edge saturated, Appl. Phys. Lett. 96 (16) (2010) 163102.
[5] O. Hod, V. Barone, J.E. Peralta, G.E. Scuseria, Enhanced half-metallicity in edge-oxidized zigzag graphene nanoribbons, Nano Lett. 7 (8) (2007) 2295–2299.
[6] K. Kusakabe, M. Maruyama, Magnetic nanographite, Phys. Rev. B 67 (9) (2003) 092406.
[7] Y.-W. Son, M.L. Cohen, S.G. Louie, Half-metallic graphene nanoribbons, Nature 444 (7117) (2006) 347.
[8] Y.-W. Son, M.L. Cohen, S.G. Louie, Energy gaps in graphene nanoribbons, Phys. Rev. Lett. 97 (21) (2006) 216803.
[9] A. Bellunato, H. Arjmandi Tash, Y. Cesa, G.F. Schneider, Chemistry at the edge of graphene, ChemPhysChem 17 (6) (2016) 785–801.
[10] G. Lee, K. Cho, Electronic structures of zigzag graphene nanoribbons with edge hydrogenation and oxidation, Phys. Rev. B 79 (16) (2009) 165440.
[11] K. Nakada, M. Fujita, G. Dresselhaus, M.S. Dresselhaus, Edge state in graphene ribbons: nanometer size effect and edge shape dependence, Phys. Rev. B 54 (24) (1996) 17954.
[12] S. Bhandary, O. Eriksson, B. Sanyal, M.I. Katsnelson, Complex edge effects in zigzag graphene nanoribbons due to hydrogen loading, Phys. Rev. B 82 (16) (2010) 165405.
[13] F. Cervantes-Sodi, G. Csanyi, S. Piscanec, A. Ferrari, Edge-functionalized and substitutionally doped graphene nanoribbons: electronic and spin properties, Phys. Rev. B 77 (16) (2008) 165427.
[14] L. Peng, K. Yao, S. Zhu, Y. Ni, F. Zu, S. Wang, B. Guo, Y. Tian, Spin transport properties of partially edge-hydrogenated MoS_2 nanoribbon heterostructure, J. Appl. Phys. 115 (22) (2014) 223705.
[15] A. Pramanik, S. Sarkar, P. Sarkar, Doped gnr p-n junction as high performance ndr and rectifying device, J. Phys. Chem. C 116 (34) (2012) 18064–18069.
[16] M. Zeng, L. Shen, M. Yang, C. Zhang, Y. Feng, Charge and spin transport in graphene-based heterostructure, Appl. Phys. Lett. 98 (5) (2011) 053101.
[17] Y. Ni, K. Yao, H. Fu, G. Gao, S. Zhu, S. Wang, Spin seebeck effect and thermal colossal magnetoresistance in graphene nanoribbon heterojunction, Sci. Rep. 3 (2013) 1380.
[18] X. Deng, Z. Zhang, G. Tang, Z. Fan, C. Yang, Spin filter effects in zigzag-edge graphene nanoribbons with symmetric and asymmetric edge hydrogenations, Carbon 66 (2014) 646–653.
[19] X. Deng, Z. Zhang, C. Yang, H. Zhu, B. Liang, The design of spin filter junction in zigzag graphene nanoribbons with asymmetric edge hydrogenation, Org. Electron. 14 (12) (2013) 3240–3248.
[20] C. Cao, L.-N. Chen, M.-Q. Long, H. Xu, Rectifying performance in zigzag graphene nanoribbon heterojunctions with different edge hydrogenations, Phys. Lett. 377 (31–33) (2013) 1905–1910.
[21] Z.-Q. Fan, W.-Y. Sun, X.-W. Jiang, J.-W. Luo, S.-S. Li, Two dimensional Schottky contact structure based on in-plane zigzag phosphorene nanoribbon, Org. Electron. 44 (2017) 20–24.

[22] J. Mahmood, E.K. Lee, M. Jung, D. Shin, I.-Y. Jeon, S.-M. Jung, H.-J. Choi, J.-M. Seo, S.-Y. Bae, S.-D. Sohn, et al., Nitrogenated holey two-dimensional structures, Nat. Commun. 6 (2015) 6486.
[23] H. Sahin, Structural and phononic characteristics of nitrogenated holey graphene, Phys. Rev. B 92 (8) (2015) 085421.
[24] Jiuyu Sun, Ruiqi Zhang, Xingxing Li, Jinlong Yang, A many-body gw+ bse investigation of electronic and optical properties of C2N, Appl. Phys. Lett. 109 (13) (2016) 133108. AIP Publishing).
[25] R. Zhang, B. Li, J. Yang, Effects of stacking order, layer number and external electric field on electronic structures of few-layer C2N-h2d, Nanoscale 7 (33) (2015) 14062–14070.
[26] S. Guan, Y. Cheng, C. Liu, J. Han, Y. Lu, S.A. Yang, Y. Yao, Effects of strain on electronic and optic properties of holey two-dimensional C2N crystals, Appl. Phys. Lett. 107 (23) (2015) 231904.
[27] D. Wang, D. Han, L. Liu, L. Niu, Structure and electronic properties of C2N/graphene predicted by first-principles calculations, RSC Adv. 6 (34) (2016) 28484–28488.
[28] M. Brandbyge, J.-L. Mozos, P. Ordejón, J. Taylor, K. Stokbro, Density-functional method for nonequilibrium electron transport, Phys. Rev. B 65 (16) (2002) 165401.
[29] H. Monkhorst, J. Pack, Special points for brillouin-zone integrations, Phys. Rev. B 13 (1976) 5188.
[30] Y. Wang, N. Song, M. Jia, D. Yang, C. Panashe, Y. Yang, J. Wang, Tunable electronic structure and magnetic moment in C2N nanoribbons with different edge functionalization atoms, Phys. Chem. Chem. Phys. 19 (23) (2017) 15021–15029.
[31] X. Wang, X. Li, L. Zhang, Y. Yoon, P.K. Weber, H. Wang, J. Guo, H. Dai, N-doping of graphene through electrothermal reactions with ammonia, Science 324 (5928) (2009) 768–771.
[32] J. Zeng, K.-Q. Chen, J. He, X.-J. Zhang, C.Q. Sun, Edge hydrogenation-induced spin-filtering and rectifying behaviors in the graphene nanoribbon heterojunctions, J. Phys. Chem. C 115 (50) (2011) 25072–25076.
[33] J. Peng, Y.-H. Zhou, K.-Q. Chen, Influence of boundary types on rectifying behaviors in hexagonal boron-nitride/graphene nanoribbon heterojunctions, Org. Electron. 27 (2015) 137–142.
[34] Y. An, K. Wang, Z. Yang, Z. Liu, G. Jia, Z. Jiao, T. Wang, G. Xu, Negative differential resistance and rectification effects in step-like graphene nanoribbons, Org. Electron. 17 (2015) 262–269.
[35] A. Jalalinia, A. Abbasi, J.J. Sardroodi, A.R. Ebrahimzadeh, The diode characteristics and rectification effect of three nanodevice containing graphene and oxidized graphene nanoribbons: a density functional theory+ non-equilibrium greens function study, Comput. Mater. Sci. 137 (2017) 125–133.